

4-point vertices from the 2PI and 4PI Effective Actions

M.E. Carrington* and Wei-Jie Fu†

*Department of Physics, Brandon University, Brandon, Manitoba, R7A 6A9 Canada and
Winnipeg Institute for Theoretical Physics, Winnipeg, Manitoba*

P. Mikula‡

*Department of Physics, University of Manitoba, Winnipeg, Manitoba, R7A 6A9 Canada and
Winnipeg Institute for Theoretical Physics, Winnipeg, Manitoba*

D. Pickering†

Department of Mathematics, Brandon University, Brandon, Manitoba, R7A 6A9 Canada

(Dated: August 9, 2018)

We consider a symmetric scalar theory with quartic coupling in 2- and 3-dimensions and compare the self-consistent 4-point vertex obtained from the 4PI effective action with the Bethe-Salpeter 4-vertex from 2PI effective action. At zero external momenta the two vertices agree well with each other when the coupling strength is small, but differences between them become more and more pronounced as the coupling strength is increased. We also study the momentum dependence of the two vertices and show that for certain momentum configurations they are almost identical, but differ for general momentum arguments.

PACS numbers: 11.10.-z, 11.15.Tk, 11.10.Kk

I. INTRODUCTION

The resummation of certain classes of Feynman diagrams to infinite loop order is a useful method in quantum field theory when there is no small expansion parameter and standard perturbative methods do not apply. A familiar example is the hard thermal loop theory [1] which was developed in the context of thermal field theory. The n PI effective action formalism [2, 3, 9, 13–16] is another approach in which the action is expressed as a functional of non-perturbative vertex functions which are determined through a self-consistent stationary equation after the effective action is expanded to some order in the loop or $1/N$ expansion. These self-consistent equations of motion resum certain classes of diagrams to infinite order, and the classes that are resummed are determined by the set of skeleton diagrams that are included in the truncated effective action.

The 2PI effective action formalism has been used to describe equilibrium thermodynamics [4, 5] and the quantum dynamics of far from equilibrium of quantum fields (see [6] and references therein). One important application is the calculation of transport coefficients [8, 11].

The 2PI theory does not contain a self-consistent 4-point vertex, but one can obtain a non-perturbative 4-point function through the Beta-Salpeter (BS) equation. It is of interest to compare this 4-vertex with the self-consistent 4-vertex from the 4PI effective action. In this paper we compare numerically the BS 4-vertex (M) obtained from the 2PI effective action and the self-consistent 4-vertex (V) from the 4PI effective action. In general the two vertices are quite different, but if we compare the BS vertex with the 4PI vertex in a specific momentum configuration $V(P, -P, K, -K)$ (which we call the “diagonal” configuration), we find good agreement between them. The conclusion

* carrington@brandonu.ca

† fuw@brandonu.ca

‡ pnmikula@gmail.com

is that for physical quantities for which the physics of the 4-point function is important, but for which diagonal momenta are expected to dominate, accurate results can be expected using the 2PI effective action. In general however, one needs the full non-perturbative 4-point function obtained from the 4PI effective action. An example is the shear viscosity which can be obtained in the large N approximation from the 2PI effective theory, but at leading order one must use a higher order effective action [12, 17, 18].

Numerical calculations in higher order n PI theories are extremely difficult and little progress has been made. One of the main obstacles is the size of the phase space involved. In this paper we develop a technique to reduce the region of the phase space that is needed to calculate V by maximally exploiting the symmetries of the vertex. This technique allows us to extend results reported in a previous paper [25] to larger lattice sizes.

This paper is organized as follows. In section II we review the n PI formalism and define our notation. In sections III we describe our numerical technique, and in IV we present results from numerical calculations in 2D and 3D. In section V we give our conclusions.

II. GENERAL FORMALISM

We consider the following Lagrangian:

$$\mathcal{L} = \frac{1}{2}(\partial_\mu \varphi \partial^\mu \varphi - m_b^2 \varphi^2) - \frac{i\lambda_b}{4!} \varphi^4. \quad (1)$$

In this equation we have introduced a scaled version of the usual coupling constant defined as $\lambda_b = -i\lambda_{\text{phys}}$ for future notational convenience. The classical action is:

$$\begin{aligned} S[\phi] &= S_0[\varphi] + S_{\text{int}}[\varphi], \\ S_0[\varphi] &= \frac{1}{2} \int d^d x d^d y \varphi(x) [iG_0^{-1}(x-y)] \varphi(y), \\ S_{\text{int}}[\varphi] &= -\frac{i\lambda_b}{4!} \int d^d x \varphi^4(x), \end{aligned} \quad (2)$$

where d denotes the number of dimensions. We use a single index to represent space-time arguments and use the summation convention to imply integration. In many equations in this paper, we suppress these indices altogether. As an example of this notation, the non-interacting part of the classical action is written:

$$\begin{aligned} S_0[\varphi] &= \frac{1}{2} \int d^d x d^d y \varphi(x) [iG_0^{-1}(x-y)] \varphi(y) = \frac{i}{2} \varphi_i G_{0,ij}^{-1} \varphi_j, \\ \rightarrow S_0[\varphi] &= \frac{i}{2} G_0^{-1} \varphi^2, \quad G_0^{-1} = -i \frac{\delta^2 S_0[\varphi]}{\delta \varphi^2} \Big|_{\varphi=0} = i(\square + m_b^2). \end{aligned} \quad (3)$$

A. 4PI effective action

The 4PI effective action is obtained from the Legendre transformation of the connected generating functional:

$$Z[R_1, R_2, R_3, R_4] = \int [d\varphi] \text{Exp}[i(S_0[\varphi] + R_1 \varphi + \frac{1}{2} R_2 \varphi^2 + \frac{1}{3!} R_3 \varphi^3 + \frac{1}{4!} R_4 \varphi^4)], \quad (4)$$

$$W[R_1, R_2, R_3, R_4] = -i \text{Ln} Z[R_1, R_2, R_3, R_4],$$

$$\Gamma[\phi, G, V_3, V_4] = W - R_1 \frac{\delta W}{\delta R_1} - R_2 \frac{\delta W}{\delta R_2} - R_3 \frac{\delta W}{\delta R_3} - R_4 \frac{\delta W}{\delta R_4}.$$

For future use we note the relations:

$$\frac{\delta W}{\delta R_1} = \langle \varphi_i \rangle = \phi, \quad (5)$$

$$2 \frac{\delta W}{\delta R_2} = \langle \varphi \varphi \rangle = G + \phi \phi. \quad (6)$$

The Legendre transforms can be done using the method of subsequent transformations [9, 14] which involves starting from an expression for the 2PI effective action and exploiting the fact that the source terms R_3 and R_4 can be combined with the corresponding bare vertex by defining a modified interaction vertex. We consider only the symmetric theory for which odd n -point functions are zero, and from now on we drop the subscript on the 4-point vertex function and write $V := V_4$. Writing the result in terms of renormalized quantities the 4-Loop 4PI effective action has the form:

$$i\Gamma[G, V] = -\frac{1}{2} \text{Tr} \ln G^{-1} - \frac{1}{2} \text{Tr} G_0^{-1} G + \Phi_0[G, V] + \Phi_{\text{int}}[G, V], \quad (7)$$

$$\Phi_0 = -\frac{1}{2} \text{Tr} \delta G_0^{-1} G + \frac{1}{8} (\lambda + \delta\lambda) G^2 + \frac{1}{4!} (\lambda + \delta\lambda) G^4 V. \quad (8)$$

We use

$$i\Gamma = \Phi = \Phi_1 + \Phi_2 = \Phi_1 + (\Phi_0 + \Phi_{\text{int}}), \quad (9)$$

where

Φ_1 is all terms with less than 2-loops and is given by the first two terms in (7)

Φ_2 is all terms with 2 or more loops

Φ_0 is the diagrams in Φ_2 which have either counter-terms or bare vertices

Φ_{int} is the remaining terms in Φ_2 (all of which have 3 or more loops)

The functional Φ_0 has the same form for $n \geq 4$ and all orders in the loop expansion, while Φ_{int} contains a set of skeleton diagrams which are determined by the order of the loop expansion. The sum of these two pieces is shown in figure 1.¹ In all diagrams, bare 4-vertices are represented by white circles, counter-terms are circles with crosses in them, and solid dots are the vertex V .

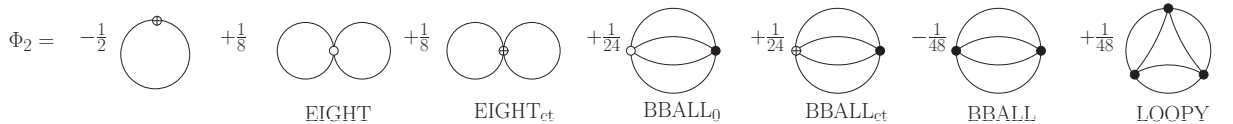


FIG. 1. $\Phi_2 = \Phi_0 + \Phi_{\text{int}}$ for the 4-Loop 4PI effective action. The open circle is a bare vertex, the circle with a cross denotes a counter-term, and the vertex V is indicated by a solid dot. The first five graphs give Φ_0 and the remaining three are Φ_{int} to 4-loops.

¹ All figures are drawn using jaxodraw [24].

The self-consistent 2- and 4-point functions in the symmetric phase are obtained by solving simultaneously the equations of motion:

$$\left. \frac{\delta \Gamma[G, V]}{\delta G} \right|_{G=\tilde{G}, V=\tilde{V}} = 0, \quad \left. \frac{\delta \Gamma[G, V]}{\delta V} \right|_{G=\tilde{G}, V=\tilde{V}} = 0. \quad (10)$$

The equation of motion for V is given in figure 2 and equation (11). We use throughout the notation $dQ = d^d q / (2\pi)^d$.

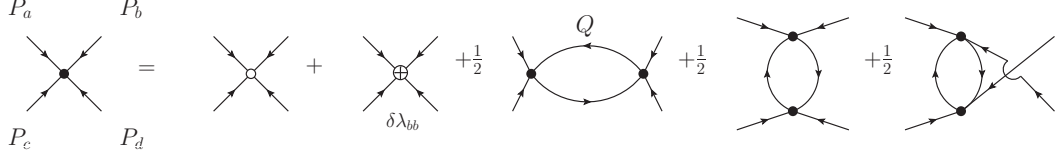


FIG. 2. Self-consistent equation of motion for the proper 4-point vertex.

$$\begin{aligned} V(P_a, P_b, P_c) &= \lambda + \delta\lambda + V_s(P_a, P_b, P_c) + V_t(P_a, P_b, P_c) + V_u(P_a, P_b, P_c), \\ V_s(P_a, P_b, P_c) &= \frac{1}{2} \int dQ V(P_a, P_c, Q) G(Q) G(Q + P_a + P_c) V(P_b, P_d, -Q), \\ V_t(P_a, P_b, P_c) &= V_s(P_a, P_c, P_b), \\ V_u(P_a, P_b, P_c) &= V_s(P_a, P_b, P_d), \quad P_d = -(P_a + P_b + P_c). \end{aligned} \quad (11)$$

The equation of motion for the 2-point function (obtained from the variational equation $\delta \Gamma / \delta G = 0$) has the form of a Dyson equation where the self-energy is proportional to the function derivative of the terms in the effective action with two and more loops:

$$G^{-1} = G_0^{-1} - \Sigma, \quad \Sigma = 2 \frac{\delta \Phi_2}{\delta G}. \quad (12)$$

The result is shown in the first line of figure 3. The diagrams can be rearranged by substituting the V equation of motion into the vertex on the left side of the sixth diagram. This substitution cancels the 3-loop diagram and produces the result in the second line of the figure and equation (13).

$$\begin{aligned} \Sigma &= - \frac{\delta \Phi_2}{\delta G} + \frac{1}{2} \text{ (loop)} + \frac{1}{2} \text{ (loop)} + (2) \frac{1}{6} \text{ (bubble)} + (2) \frac{1}{6} \text{ (bubble)} - \frac{1}{6} \text{ (bubble)} + \frac{1}{4} \text{ (3-loop)} \\ &= - \frac{\delta \Phi_2}{\delta G} + \frac{1}{2} \text{ (loop)} + \frac{1}{2} \text{ (loop)} + \frac{1}{6} \text{ (bubble)} + \frac{1}{6} \text{ (bubble)} \end{aligned}$$

FIG. 3. The self-energy obtained from equations (7) and (12).

$$\Sigma(P) = i(\delta Z P^2 - \delta m^2) + \frac{1}{2}(\lambda + \delta\lambda) \int dQ G(Q)$$

$$+ \frac{1}{6}(\lambda + \delta\lambda_{\text{bb}}) \int dQ \int dK V(P, Q, K) G(Q) G(K) G(Q + K + P). \quad (13)$$

B. 2PI Bethe-Salpeter Equation

Although the 2PI effective action does not explicitly contain a 4-vertex, it is well known that it can be used to obtain a non-perturbative 4-point vertex called the Bethe-Salpeter vertex [19]. The equation that determines the 2PI BS vertex is obtained by calculating the functional derivatives of the 2PI effective action with respect to the 2-point function G_{kl} and the bilocal source. In order to avoid unnecessary subscripts, we use J and R to represent the external sources R_1 and R_2 in the 2PI effective action.

Using Eqs. (4) and (9) we have directly

$$\frac{\delta}{\delta R_{ij}} \frac{\delta}{\delta G_{kl}} \Phi = -\frac{i}{4}(\delta_{ik}\delta_{jl} + \delta_{il}\delta_{jk}). \quad (14)$$

The derivatives on the left side of (14) can also be written

$$\frac{\delta}{\delta R_{ij}} \frac{\delta}{\delta G_{kl}} \Phi = \frac{\delta\phi_x}{\delta R_{ij}} \frac{\delta^2\Phi}{\delta\phi_x\delta G_{kl}} + \frac{\delta G_{xy}}{\delta R_{ij}} \frac{\delta^2\Phi}{\delta G_{xy}\delta G_{kl}}. \quad (15)$$

Since we consider only the symmetric theory, we drop all terms that correspond to vertices with an odd number of legs, which means that only the second term on the right side survives. Using (9) we write:

$$\begin{aligned} 4 \frac{\delta^2\Phi}{\delta G_{xy}\delta G_{kl}} &= 4 \frac{\delta^2\Phi_1}{\delta G_{xy}\delta G_{kl}} + 4 \frac{\delta^2\Phi_2}{\delta G_{xy}\delta G_{kl}}, \\ &=: \Lambda_{xykl}^{disco} + \Lambda_{xykl} = -(G_{xk}^{-1}G_{yl}^{-1} + G_{xl}^{-1}G_{yk}^{-1}) + \Lambda_{xykl}. \end{aligned} \quad (16)$$

The term Λ_{xykl}^{disco} represents all disconnected contributions and comes from the 1-loop terms in the effective action, and Λ_{xykl} contains all contributions from Φ_2 . The derivative of the propagator with respect to the source R is:

$$\begin{aligned} \frac{\delta G_{xy}}{\delta R_{ij}} &= \frac{\delta}{\delta R_{ij}} (\langle \varphi_x \varphi_y \rangle - \langle \varphi_x \rangle \langle \varphi_y \rangle), \\ &= \frac{i}{2} (\langle \varphi_x \varphi_y \varphi_i \varphi_j \rangle - \langle \varphi_x \varphi_y \rangle \langle \varphi_i \varphi_j \rangle + \dots), \\ &= \frac{i}{2} (G_{ia} G_{jb} G_{xc} G_{yd} M_{abcd} + G_{ix} G_{jy} + G_{iy} G_{jx} + \dots), \end{aligned} \quad (17)$$

where the dots indicate expectation values which contain an odd number of field operators and are zero in the symmetric theory. Substituting equations (16) and (17) into (15) and setting the result equal to the expression obtained in (14) we have:

$$0 = \frac{i}{4} G_{ix} G_{jy} (-M_{klxy} + \Lambda_{klxy} + \frac{1}{2} \Lambda_{klab} G_{ac} G_{bd} M_{cdxy}), \quad (18)$$

where we have used the fact that the vertices Λ_{klxy} and M_{klxy} are symmetric with respect to permutations of the first two indices, or the second two indices, or the interchange of the first pair and

the second pair: $\Lambda_{klxy} = \Lambda_{lkxy} = \Lambda_{klyx} = \Lambda_{xykl}$. Truncating the external legs we obtain the standard form of the BS equation:

$$M_{xykl} = \Lambda_{xykl} + \frac{1}{2} \Lambda_{xyab} G_{ac} G_{bd} M_{cdkl}. \quad (19)$$

We consider systems in thermal equilibrium for which the system is invariant under space-time translations and write equation (19) in momentum space as:

$$M(P, -P, Q, -Q) = \Lambda(P, -P, Q, -Q) + \frac{1}{2} \int dK \Lambda(P, -P, K, -K) G^2(K) M(K, -K, Q, -Q). \quad (20)$$

We will refer to the momentum arguments in Eq. (20) as “diagonal.” Equation (20) is shown diagrammatically in figure 4.

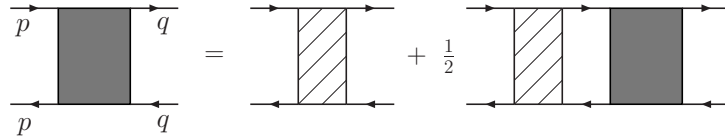


FIG. 4. Diagrammatic representation of the BS equation in equation (20). Grey boxes and boxes with oblique lines in them represent the vertex M and kernel Λ , respectively.

III. NUMERICAL CALCULATIONS ON A LATTICE

A. Discretization and the Relaxation Method

We solve the self-consistent equations of motion for the 2- and 4-point functions using a numerical lattice method [25]. The first step is to rotate to Euclidean space. We define the Euclidean variables:

$$\begin{aligned} q_0 &= iq_E, \quad \delta Z = \delta Z_E, \quad \delta m^2 = \delta m_E^2, \quad G = -iG_E, \quad \Sigma = -i\Sigma_E, \\ \lambda &= -i\lambda_E, \quad \delta\lambda = -i\delta\lambda_E, \quad V = iV_E, \quad M = iM_E. \end{aligned} \quad (21)$$

Note that the factor i in the definition of the Euclidean vertex removes the i introduced in the definition of λ_b in Eq. (1). The Dyson equation in Euclidean space is (see equation (12)):

$$G_E^{-1}(P) = G_{0E}^{-1}(P) + \Sigma_E(P). \quad (22)$$

All variables from here on are Euclidean and we suppress the subscript E . The coupling constant and 4-point vertex have dimension $4 - d$ so that in 2D $\lambda \sim m^2$ and in 3D $\lambda \sim m$.

There are no ultra-divergences in the 4-point vertices in less than four dimensions, and therefore we choose the coupling strength counter-term to be vanishing, i.e., $\delta\lambda = 0$. For the 2-point function, the only fundamental divergences are the tadpole and sunset diagrams. The tadpole diagram has a momentum independent divergence in 2D and is finite in 3D. The sunset diagram is finite in 2D and has a momentum independent divergence in 3D. Since we have no momentum dependent divergences, we can also set $\delta Z = 0$ and renormalize the propagator with the counter-term δm^2 . To determine this counter-term we use the renormalization condition $\Sigma(0) = 0$, which means we can drop the tadpole diagram. Note that if one expands the equation of motion for the 4-vertex

V obtained from the 4PI effective action, or the equation for the BS vertex from the 2PI effective action, each self-energy insertion is accompanied by the mass counter-term that makes it finite, and therefore there are no sub-divergences.

We use an N^d symmetric lattice with periodic boundary conditions. In 2D we use N up to 16 and in 3D N up to 12. The lattice spacing is a and we choose $a = 2\pi/(Nm)$. In Euclidean space, each momentum component is discretized:

$$Q_i = \frac{2\pi}{aN} n_i = m n_i, \quad n_i = -\frac{N}{2} + 1, \dots, \frac{N}{2}. \quad (23)$$

Indices which fall outside of the range $\{-N/2 + 1, N/2\}$ are wrapped inside using periodic boundary conditions. This is done using the function

$$\text{rndx}[\text{index}] = 1 - N/2 + \text{Mod}[\text{index} + N/2 - 1, N], \quad (24)$$

where $\text{Mod}[m, n]$ is an integer function that gives the remainder on division of m by n so that $0 < \text{Mod}[m, n] < n - 1$ (for example, $\text{Mod}[17, 17] = 0$ and $\text{Mod}[23, 17] = 6$). To illustrate we consider $N = 4$. Integers outside the range $\{-1, 0, 1, 2\}$ are wrapped into this range periodically using the function in Eq. (24):

$$\begin{aligned} & \vdots \\ & \{\text{rndx}[-5], \text{rndx}[-4], \text{rndx}[-3], \text{rndx}[-2]\} \rightarrow \{-1, 0, 1, 2\} \\ & \{\text{rndx}[-1], \text{rndx}[0], \text{rndx}[1], \text{rndx}[2]\} \rightarrow \{-1, 0, 1, 2\} \\ & \{\text{rndx}[3], \text{rndx}[4], \text{rndx}[5], \text{rndx}[6]\} \rightarrow \{-1, 0, 1, 2\} \\ & \vdots \end{aligned}$$

We scale all dimensional quantities by the mass, or equivalently set $m = 1$ and use mass units for all variables that carry dimension. Using this notation the size of the box in co-ordinate space $L = aN$ is fixed, and the maximum momentum is $p_{\text{max}} = N/2$.

On the lattice, the 4PI equations of motion become:

$$\begin{aligned} V(P_a, P_b, P_c) = & -\lambda + \frac{1}{2} \frac{1}{(aN)^d} \sum_Q \left[V(P_a, P_c, Q) G(Q) G(Q + P_a + P_c) V(P_b, P_d, -Q) \right. \\ & + V(P_a, P_b, Q) G(Q) G(Q + P_a + P_b) V(P_c, P_d, -Q) \\ & \left. + V(P_a, P_d, Q) G(Q) G(Q + P_a + P_d) V(P_b, P_c, -Q) \right]. \end{aligned} \quad (25)$$

$$\Sigma_{4\text{PI}}(P) = \delta m^2 + \frac{1}{6} \lambda \frac{1}{(aN)^{2d}} \sum_Q \sum_K V(P, Q, K) G(Q) G(K) G(Q + K + P). \quad (26)$$

In the 2PI formalism, we truncate the effective action at 3-Loops. The self-energy contains the tadpole and sunset diagrams as in figure 3, but with all vertices bare. On the lattice we have

$$\Sigma_{2\text{PI}}(P) = \delta m^2 - \frac{1}{6} \lambda^2 \frac{1}{(aN)^{2d}} \sum_Q \sum_K G(Q) G(K) G(Q + K + P). \quad (27)$$

The kernel Λ contains the bare vertex and the t - and u -channel 1-loop diagrams (the third and fifth diagrams in figure 2) with bare vertices. Abbreviating the momentum arguments $(P, -P, Q, -Q)$ as (P, Q) we have

$$\Lambda(P, Q) = -\lambda + \frac{\lambda^2}{2} \frac{1}{(aN)^d} \sum_K G(K)G(K+P-Q) + \frac{\lambda^2}{2} \frac{1}{(aN)^d} \sum_K G(K)G(K+P+Q), \quad (28)$$

and the BS equation in Eq. (20) is

$$M(P, Q) = \Lambda(P, Q) + \frac{1}{2} \frac{1}{(aN)^d} \sum_K \Lambda(P, K)G^2(K)M(K, Q). \quad (29)$$

We use a numerical iterative method to solve the set of self-consistent equations, for both the 2PI and 4PI theories. A naive implementation of this method would be as follows.

2PI: On the right side of the 2PI equations (27)-(29) one starts using $G(P) = G_{\text{in}}(P) = G_0(P)$ and $M(P, K) = M_{\text{in}}(P, K) = \Lambda(P, K)$. The first iteration of the calculation then produces $G_{\text{out}}(P)$ and $M_{\text{out}}(P, K)$. One defines

$$\begin{aligned} G_{\text{up}}(P) &= \alpha G_{\text{out}}(P) + (1 - \alpha)G_{\text{in}}(P), \\ M_{\text{up}} &= \alpha M_{\text{out}}(P, K) + (1 - \alpha)M_{\text{in}}(P, K), \end{aligned} \quad (30)$$

and then uses these updated values as input for the second iteration. The parameter $1 > \alpha > 0$ is chosen to improve convergence.

4PI: On the right side of the 4PI equations (25) and (26) one starts with $G(P) = G_{\text{in}}(P) = G_0(P)$ and $V(P, K, Q) = V_{\text{in}}(P, K, Q) = -\lambda$ and first iteration of the calculation produces $G_{\text{out}}(P)$ and $V_{\text{out}}(P, K, Q)$. The updated values are

$$\begin{aligned} G_{\text{up}}(P) &= \alpha G_{\text{out}}(P) + (1 - \alpha)G_{\text{in}}(P), \\ V_{\text{up}}(P, K, Q) &= \alpha V_{\text{out}}(P, K, Q) + (1 - \alpha)V_{\text{in}}(P, K, Q). \end{aligned} \quad (31)$$

The procedure we use to calculate V is slightly different from what is described above. Using the “naive” method would mean that after having calculated V_{out} , but before updating, we would have values V_{out} and V_{in} at all points of the phase space. For large values of N memory constraints are an issue and therefore we use an in-place updating in which equation (31) is used at each point in phase space as the computation proceeds. Mathematically one is iteratively searching for fixed points and point-wise convergence is faster using in-place updates.

The calculation is continued until the relative maximum difference between the input and output values at all points in momentum space is less than 10^{-4} . We use $\alpha = 0.8$ and obtain convergence in less than 10 iterations, depending on the value of λ .

B. Time and Memory Constraints

The number of points in the phase space of a vertex is given generically by $N^{l \times d}$ where l is the number of independent momenta and d is the dimension. For the vertex M one can fix the

momentum on one side of the vertex, because of the fact that the BS equation resums only one channel: if one wants to calculate $M(P, Q_{\text{fixed}})$ for any choice Q_{fixed} one can solve Eq. (29) in the form

$$M(P, Q_{\text{fixed}}) = \Lambda(P, 0) + \frac{1}{2} \frac{1}{(aN)^d} \sum_K \Lambda(P, K) G^2(K) M(K, Q_{\text{fixed}}). \quad (32)$$

The phase space for the vertex M is therefore $N^{1 \times d}$ in spite of the fact that there are two independent momenta.

The sets of self-consistent equations we are solving contain $V(P, K, Q)$, $M(P, Q_{\text{fixed}})$, $G(P)$ and $\Sigma(P)$, but the phase space of the vertex V is the largest by a huge factor, and therefore it is the limiting factor in terms of both memory and computing time. In this section we describe how one can reduce the size of the phase space of V using the symmetries of the vertex. For the remainder of this section we specialize to three dimensions.

We represent the arguments of the 4-point function $V(P, K, Q)$ by a 3×3 matrix of the form

$$\mathbf{P} = \begin{pmatrix} p_x & p_y & p_z \\ k_x & k_y & k_z \\ q_x & q_y & q_z \end{pmatrix}. \quad (33)$$

Since momentum is conserved the fourth leg of the vertex has momentum $(-(p_x + k_x + q_x), -(p_y + k_y + q_y), -(p_z + k_z + q_z))$. This gives us a matrix of four rows which we denote \mathbf{P}^π and call the augmented matrix of \mathbf{P} . The fourth row appears to be redundant but leads to significant gains in computational efficiency, as will be explained below.

$$\mathbf{P}^\pi = \begin{pmatrix} p_x & p_y & p_z \\ k_x & k_y & k_z \\ q_x & q_y & q_z \\ -(p_x + k_x + q_x) & -(p_y + k_y + q_y) & -(p_z + k_z + q_z) \end{pmatrix} = \begin{pmatrix} p_x & p_y & p_z \\ k_x & k_y & k_z \\ q_x & q_y & q_z \\ l_x & l_y & l_z \end{pmatrix}. \quad (34)$$

The values $l_x = -(p_x + k_x + q_x)$, $l_y = -(p_y + k_y + q_y)$, and $l_z = -(p_z + k_z + q_z)$ are not necessarily in the range $\{-N/2 + 1, N/2\}$, and therefore whenever we go from \mathbf{P} to the augmented matrix \mathbf{P}^π the reindex function is invoked.

Vertices are symmetric under interchange of legs and therefore any three rows of the augmented matrix \mathbf{P}^π represent the same V . The vertices have other symmetries as well: rotational symmetry means columns can be interchanged, and inversion symmetry allows any column to be replaced by its negative. We want to take advantage of these symmetries to reduce computation time and memory requirements. The complete set of N^9 matrices \mathbf{P} can be grouped into blocks (partitions) satisfying $V(\mathbf{P}_\alpha) = V(\mathbf{P}_\beta)$ for any \mathbf{P}_α and \mathbf{P}_β in the same partition. Two matrices \mathbf{P} and \mathbf{P}' are in the same partition if \mathbf{P}' can be obtained from \mathbf{P} by the following procedure.

1. Given \mathbf{P} form the augmented matrix \mathbf{P}^π (reindexing if necessary).
2. Use any number of the following operations in any order.
 - (a) Interchange any rows of \mathbf{P}^π (leg symmetry)
 - (b) Interchange any columns of \mathbf{P}^π (rotational symmetry)
 - (c) Multiply any column(s) of \mathbf{P}^π by -1 (inversion symmetry)

Reindexing is sometimes necessary because $-N/2 \notin \{-N/2 + 1, N/2\}$.

3. Choose any three rows of \mathbf{P}^π to obtain \mathbf{P}'

For example ($N = 6$), the matrices \mathbf{P} , \mathbf{P}' and \mathbf{P}'' in equation (35) are in the same partition. Note that the value 3, not present in \mathbf{P} , appears in \mathbf{P}' and \mathbf{P}'' , which demonstrates the advantage of using the augmented matrix.

$$\mathbf{P} = \begin{pmatrix} -2 & 0 & 1 \\ -1 & 1 & 0 \\ 0 & 0 & -2 \end{pmatrix}, \quad \mathbf{P}^\pi = \begin{pmatrix} -2 & 0 & 1 \\ -1 & 1 & 0 \\ 0 & 0 & -2 \\ 3 & -1 & 1 \end{pmatrix}, \quad \mathbf{P}' = \begin{pmatrix} -1 & 1 & 0 \\ 3 & -1 & 1 \\ 0 & 0 & -2 \end{pmatrix}, \quad \mathbf{P}'' = \begin{pmatrix} 2 & 0 & -1 \\ 1 & 1 & 0 \\ 3 & -1 & -1 \end{pmatrix}. \quad (35)$$

If we define $\mathbf{P} \approx \mathbf{P}'$ whenever \mathbf{P}' can be obtained from \mathbf{P} using the procedure described above, then \approx is an equivalence relation on the set of all 3×3 matrices with entries in $\{-N/2+1, N/2\}$. The minimal sized partition of this equivalence relation is 1, when \mathbf{P} is the zero matrix. The maximal sized partitions are of cardinality $1152 = (4!)(3!)(2^3)(4)$, since there are $4!$ ways to interchange rows, $3!$ ways to interchange columns, 2^3 ways to multiply column(s) by -1 , and 4 ways to choose three rows from a set of four. Partitions are bigger when N is bigger because reindexing occurs less often for large N . When $N = 12$ the average size of a partition is approximately 1000.

We need only compute V for a single element of each partition, since $V(\mathbf{P}_\alpha) = V(\mathbf{P}_\beta)$ if $\mathbf{P}_\alpha \approx \mathbf{P}_\beta$. This reduces the main iteration loop by a factor of approximately the average size of a partition. The storage requirements for V are reduced by the same factor. The table below shows the size of the phase space and the number of representative points that need to be calculated for $d = 3$ and different values of N .

N	$N^{3 \cdot (d=3)}$	smallest # of reps
6	10,077,696	11,424
8	134,217,728	129,502
10	1,000,000,000	913,661
12	5,159,780,352	4,608,136

We choose a unique element from each partition and call it the representative of that partition, abbreviated **repr** or **repr**(\mathbf{P}). We need a list containing one representative from each partition to set up the main iterative loop which calculates $V_{\text{out}}(\mathbf{repr}(\mathbf{P}))$. The sums in equation (25) range over all possible \mathbf{P} and therefore in the iterative calculation of $V_{\text{out}}(\mathbf{repr}(\mathbf{P}))$ one needs vertices $V_{\text{in}}(\mathbf{P})$ which were not calculated in the previous iteration. Inside the summation we must replace $V_{\text{in}}(\mathbf{P})$ with $V_{\text{in}}(\mathbf{repr}(\mathbf{P}))$. The representative-finding function must be fast because it is the most frequently hit part of the computation and is the limiting factor in the running time of the program.

Our first attempt was as follows. For each element \mathbf{P} , generate the partition containing \mathbf{P} , sort the partition, and choose its minimal element as the representative. Save the list of representatives and use it to determine which values of V_{out} to calculate. The same calculation of **repr**(\mathbf{P}) must be done over and over again on the right side of the equation for V_{out} inside the summation over V_{in} 's. The process of generating, sorting and minimizing 1152 matrices cannot be done N^9 times for large N .

A better method is to find a function “**vindex**” that computes an integer for each \mathbf{P} which is then used to “address” the value of $V_{\text{out}}(\mathbf{P})$. The function **vindex** should satisfy the conditions

$$\mathbf{vindex}(\mathbf{P}_i) = \mathbf{vindex}(\mathbf{P}_j) \quad \text{if} \quad \mathbf{P}_i \approx \mathbf{P}_j, \quad (36)$$

$$\mathbf{vindex}(\mathbf{P}_i) \neq \mathbf{vindex}(\mathbf{P}_j) \quad \text{if} \quad \mathbf{P}_i \not\approx \mathbf{P}_j. \quad (37)$$

Equation (36) says that **vindex** is the same for every element of a partition, and (37) says that **vindex** is different for any two matrices which belong to different partitions.

We start by explaining how to construct the function **vindex** so that (36) is satisfied. For a given augmented matrix \mathbf{P}^π the following functions are constant if rows or columns are interchanged.

- $f_1(\mathbf{P}^\pi) = p_x + k_x + q_x + l_x + p_y + k_y + q_y + l_y + p_z + k_z + q_z + l_z$
- $f_2(\mathbf{P}^\pi) = p_x k_x q_x l_x p_y k_y q_y l_y p_z k_z q_z l_z$
- $f_3(\mathbf{P}^\pi) = (p_x k_x q_x l_x) + (p_y k_y q_y l_y) + (p_z k_z q_z l_z)$
- $f_4(\mathbf{P}^\pi) = (p_x + k_x + q_x + l_x)(p_y + k_y + q_y + l_y)(p_z + k_z + q_z + l_z)$
- $f_5(\mathbf{P}^\pi) = (p_x + p_y + p_z)(k_x + k_y + k_z)(q_x + q_y + q_z)(l_x + l_y + l_z)$
- $f_6(\mathbf{P}^\pi) = p_x p_y p_z + k_x k_y k_z + q_x q_y q_z + l_x l_y l_z$

We define

$$g(\mathbf{P}^\pi) = f_1(\mathbf{P}^\pi) \cdot f_3(\mathbf{P}^\pi) + f_5(\mathbf{P}^\pi) + f_6(\mathbf{P}^\pi), \quad (38)$$

$$n_i = g(\mathbf{P}^\pi), \quad 1 \leq i \leq 8 \text{ for 8 ways to multiply columns by } \{0, 1, 2, 3\}, -1's, \quad (39)$$

$$\mathbf{vindex}(\mathbf{P}) = \text{Mod}(\text{Max}\{n_i\} + \text{Min}\{n_i\} + \sum_{i=1}^8 n_i, \mathbf{nprime}), \quad (40)$$

where (**nprime**) is a large prime which is chosen to correspond approximately to the available physical computer memory. The computed set of numbers $\{n_i\}$ is the same for every element of a partition and therefore $\mathbf{vindex}(\mathbf{P}_i) = \mathbf{vindex}(\mathbf{P}_j)$ for any two $\mathbf{P}_i \approx \mathbf{P}_j$, which means that equation (40) satisfies the condition (36).

However, equation (40) does not always satisfy (37). A “collision” occurs if $\mathbf{P}_i \not\approx \mathbf{P}_j$ but $\mathbf{vindex}(\mathbf{P}_i) = \mathbf{vindex}(\mathbf{P}_j)$. In practice, results are numerically indistinguishable whenever the number of collisions is less than approximately 5% of the total size of the set of representatives. The functions f_i above, the combinations of the f_i ’s which make g , and the combinations of the n_i ’s which give **vindex** (equation (40)), are chosen so that the number of collisions is small. We have checked that our results are not affected by collisions by including additional functions in the set of f_i and in g to reduce the number of collisions. We have also run our program using a recursive definition of **vindex** with a different choice **nprime** in the event of a collision, which reduces the number of collisions to almost zero. For small N ’s one can also check the results produced using the indexing method by comparing with the original sorting/minimizing method.

IV. NUMERICAL RESULTS

In this section we present our results.

Figure 5 compares the 4PI self-consistent 4-vertex V , the 2PI BS 4-vertex M , and the perturbative 4-vertex, as functions of the coupling strength. The momentum arguments are chosen to be vanishing. The perturbative calculation is done with the self-consistent vertex and the propagator on the right

hand side of Eq. (25) replaced by the bare ones. The 4PI and 2PI calculations in 2D are performed with $N = 16, 12$, and 8 , and in 3D with $N = 12, 10$, and 8 . The perturbative calculation is done in 2D with $N = 16$ and in 3D with $N = 12$. When the coupling λ is small, V agrees well with M and the perturbative 4-vertex, but the differences between them become larger as λ increases, and differences are larger in 2D than 3D. The 2D perturbative vertex becomes negative when λ is large enough, which shows that the 1-loop contribution has overwhelmed the tree term. The vertex M lies between V and the perturbative result for all values of coupling.

In Fig. 6 we look at the self-energy $\Sigma(P)$ obtained from the 4PI, 2PI, and perturbative calculations. We show the dependence on P_x with all other momentum components set to zero. The 2PI self-energy agrees well with the perturbative one when $\lambda = 5$ (in Ref. [25] it was shown that a significant difference between the 2PI self-energy and the perturbative one appears at very large λ). The 4PI self-energy is smaller than the 2PI and perturbative self-energies at nonvanishing external momentum.

Figure 7 compares the dependence of V and M on one momentum component $(P_a)_x$, with all other external momentum components set to zero. The difference between V and M is maximal at $(P_a)_x = 0$, and decreases with increasing $(P_a)_x$. We find again that M lies between V and the perturbative vertex, in this case for all momenta. The right side of the figure shows that the differences between the three vertices is larger when λ is larger. The perturbative result deviates strongly from V and M at large λ , even when the external momentum is large.

We also compare the vertices V and M for different momentum configurations. In Fig. 8 we show V in 2D and 3D as a function of $(P_a)_x$ and $(P_b)_x$ with all other momenta components set to zero, including all components of $P_c = 0$. In 3D this can be written $(P_a; P_b; P_c) \rightarrow ((P_a)_x, 0, 0; (P_b)_x, 0, 0; 0, 0, 0)$.

The right side of Fig. 9 is a plot of $M((P_a)_x, 0, 0; -(P_b)_x, 0, 0)$ (P_b is defined as positive coming into the vertex V , whereas the upper right leg of the vertex M carries momentum Q defined as outgoing). Note that the curves shown in Fig. 7 correspond to horizontal lines on the contour plots in figures 8 and the right side of figure 9, starting at the centre of and continuing to the right edge. The graphs on the right side of Fig. 9 look very different from those of Fig. 8. The left side of Fig 9 shows a contour plot of V with diagonal momentum components $(P_a; P_b; P_c) \rightarrow ((P_a)_x, 0, 0; (P_b)_x, 0, 0; -(P_a)_x, 0, 0)$. Comparison of the left and right sides of Fig 9 shows that V in a diagonal momentum configuration agrees well with M .

In Fig. 10 we look explicitly at the difference

$$M((P_a)_x, 0, 0; -(P_b)_x, 0, 0) - V((P_a)_x, 0, 0; (P_b)_x, 0, 0; -(P_a)_x, 0, 0).$$

The graph shows that $M - V$ is largest along the two lines which run from the upper right corner to the lower left corner, and from upper left to lower right, or the lines given by $(P_a)_x = \pm(P_b)_x$. The word ‘diagonal’ has already been used to denote the configuration $P_a = P$, $P_b = -Q$, $P_c = -P$ and therefore we call the lines $(P_a)_x = \pm(P_b)_x$ the \times diagonal region. The difference $M - V$ is smallest along the horizontal and vertical lines that pass through the center of the graph, except for the neighbourhood of the point where these lines cross. Mathematically we have that $M - V$ is smallest for $(P_a)_x = 0$ and $(P_b)_x \neq 0$, or $(P_b)_x = 0$ and $(P_a)_x \neq 0$. We call this the $+$ diagonal region.

We would like to understand why the difference between V and M is largest in the \times diagonal region and smallest in the $+$ diagonal region. The vertex M is a resummation in the s -channel of the kernel Λ , which contains the 1-loop t - and u -channels. The vertex M therefore includes s -channels to all orders, but only the 1-loop diagrams in the t - and u - channels. The equation of motion for the vertex V is a symmetric resummation in all three channels, and therefore contains s - t - and u -channels to all orders. In order to understand the relative size of M and V in different momentum

regimes, we look at the contributions from each channel.

The three 1-loop graphs shown in Fig. 2 which are, in order, the s - t - and u -channels. For definiteness we choose one line in the \times diagonal and $+$ diagonal regions:

$$\begin{aligned} \times\text{diagonal} : \quad (P_a)_x &= -(P_b)_x, \\ +\text{diagonal} : \quad (P_a)_x &\neq 0, \quad = \pm(P_b)_x = 0. \end{aligned} \tag{41}$$

In Table 1 we give the momentum arguments of the two propagators in each channel using K for the loop momentum.

	s	t	u
general $V(P_a, P_b, P_c, -P_a - P_b - P_c)$	$K(K + P_a + P_c)$	$K(K + P_a + P_b)$	$K(K - P_b - P_c)$
diagonal $V(P_a, P_b, -P_a, -P_b)$	$K(K)$	$K(K + P_a + P_b)$	$K(K + P_a - P_b)$
\times diagonal $V(P_a, -P_a, -P_a, P_a)$	$K(K)$	$K(K)$	$K(K + 2P_a)$
$+$ diagonal $V(P_a, 0, -P_a, 0)$	$K(K)$	$K(K + P_a)$	$K(K + P_a)$

Our results indicate that diagrams with propagators of the form $G(K)^2$ will give a larger contribution than diagrams with propagators $G(K)G(K + K')$. This can be seen as follows. In the \times diagonal region the s - and t -channels both contain a factor $G(K)^2$ and therefore their contributions will be greater than that of the u -channel. Since V contains a t -channel resummation and M does not, we expect $M - V$ large in this region. In the $+$ diagonal region the largest contribution comes from the s -channel. Since both V and M include an infinite resummation in the s -channel, we expect the difference between them to be small.

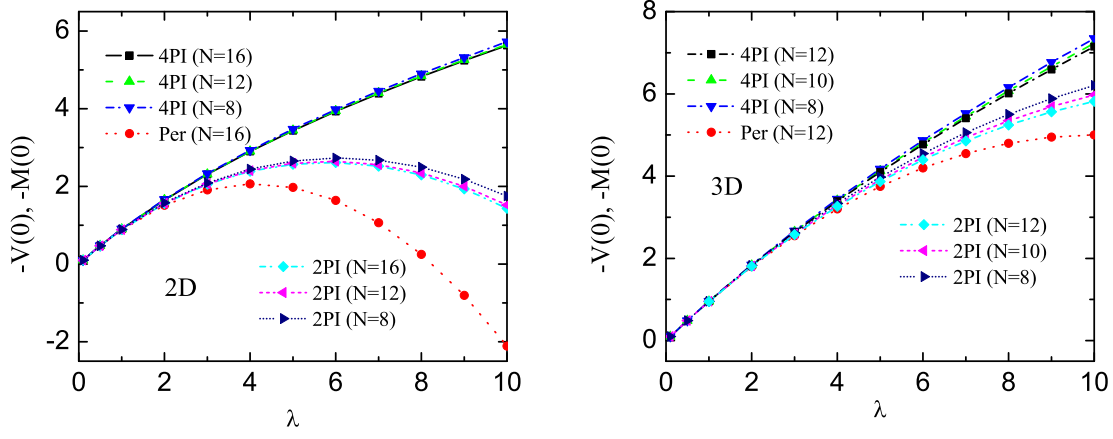


FIG. 5. (color online). Comparison of V and M as functions of the coupling strength λ . All the momentum arguments are chosen to be vanishing. The calculations are done in 2D with $N = 16, 12$, and 8 (left panel), and in 3D with $N = 12, 10$, and 8 (right panel). For comparison we also show the perturbative result in each graph, which is the dotted line joining round markers (red).

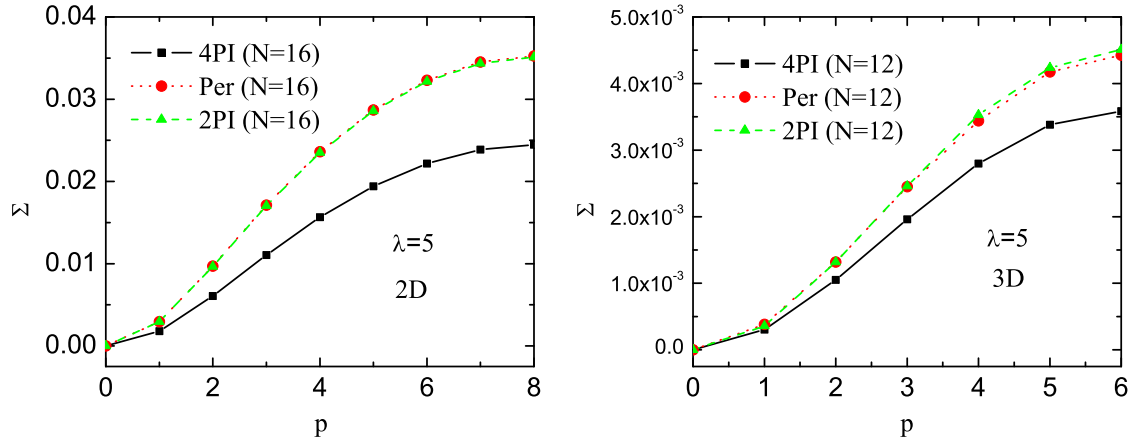


FIG. 6. (color online). Comparison of the dependence of the 4PI and 2PI self-energies on P_x with all other momentum components set to zero. Calculations are done in 2D with $N = 16$ (left panel) and in 3D with $N = 12$ (right panel), and $\lambda = 5$.

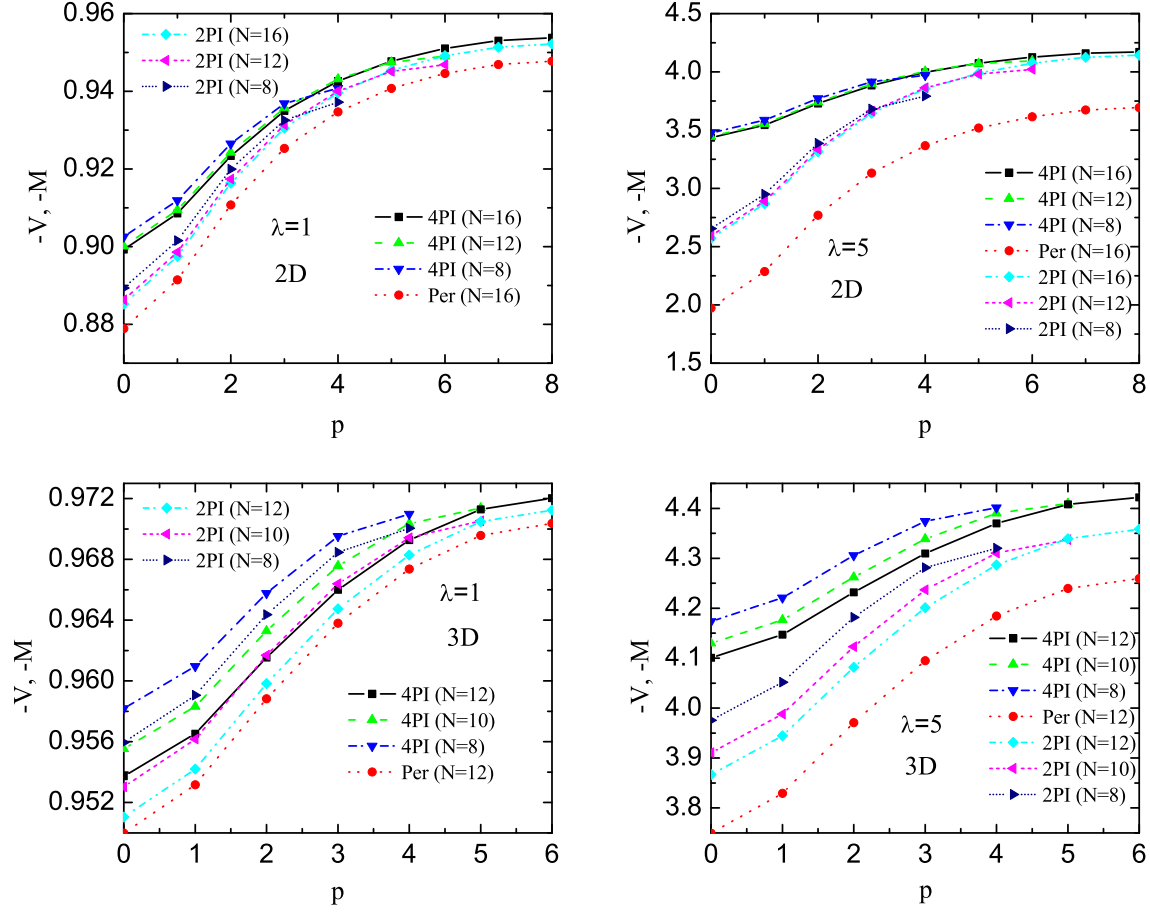


FIG. 7. (color online). Comparison of the dependence of V and M on $(P_a)_x$ with all other external momentum components set to zero. Top left panel is 2D with $\lambda = 1$, top right is 2D with $\lambda = 5$, bottom left is 3D with $\lambda = 1$, and bottom right is 3D with $\lambda = 5$. The perturbative result is the dotted line which joins round markers (red).

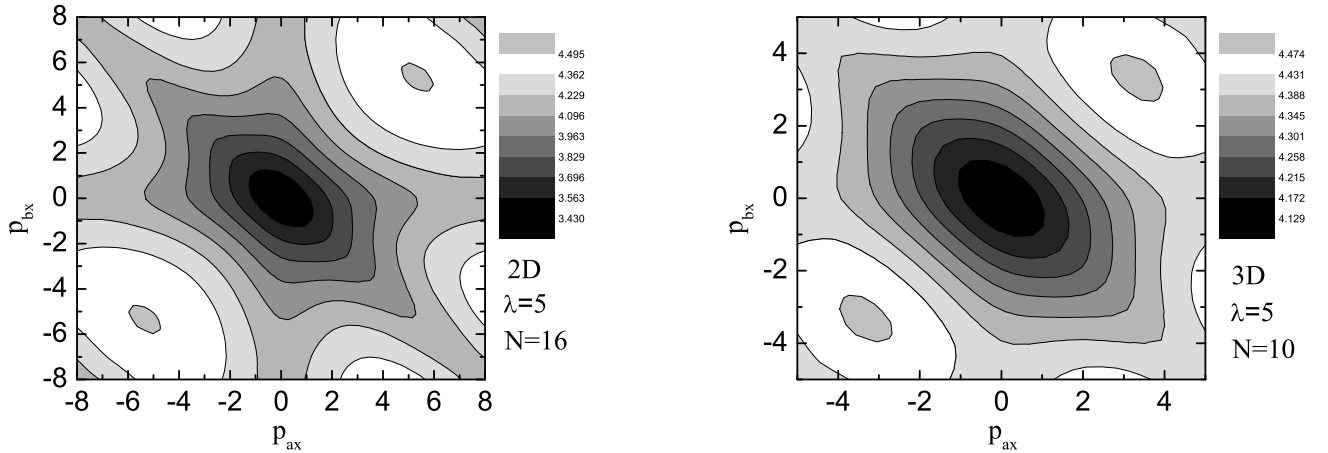


FIG. 8. Contour plot of V in 2D and 3D as a function of $(P_a)_x$ and $(P_b)_x$ with all other momenta components set to zero for $\lambda = 5$.

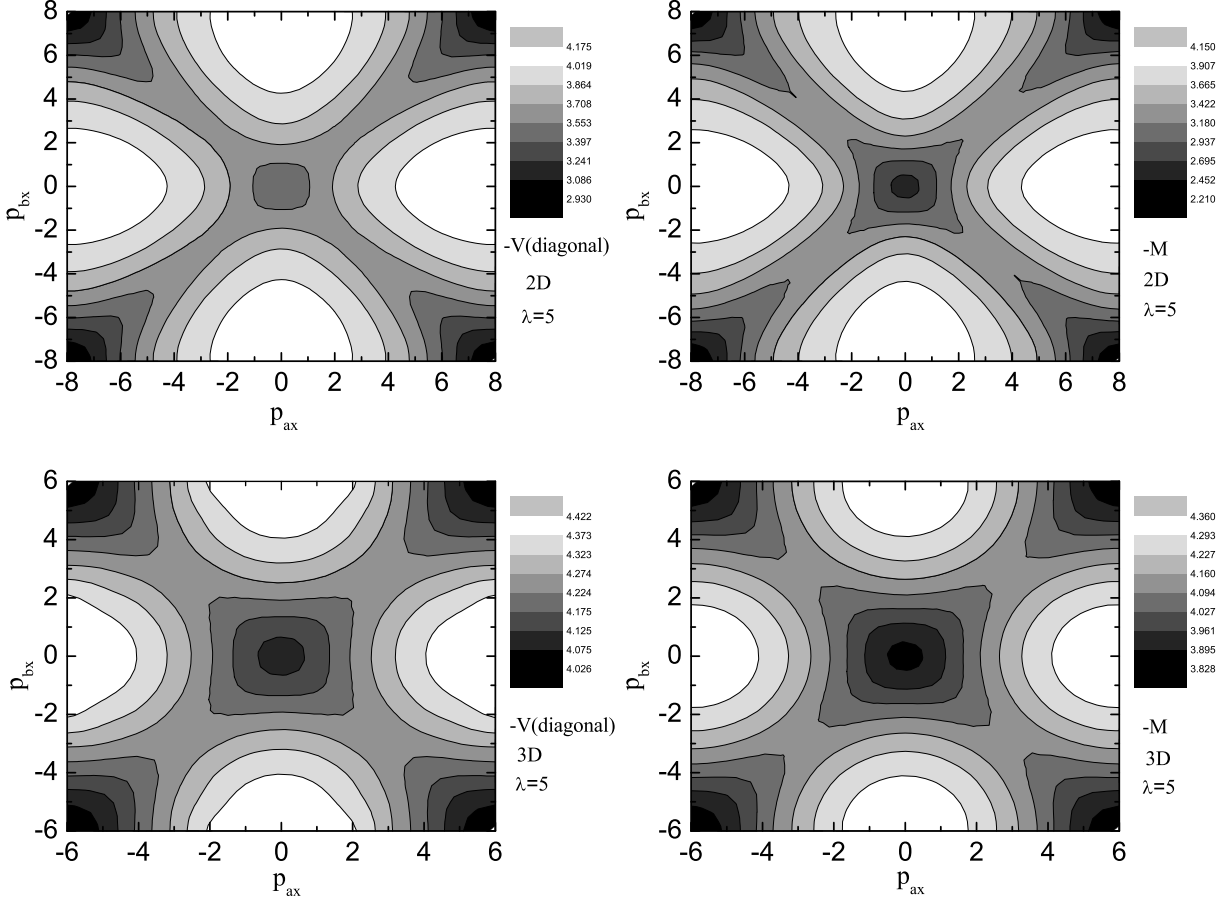


FIG. 9. Contour plot of $V((P_a)_x, (P_b)_x, (P_c)_x = -(P_a)_x)$ and $M((P_a)_x, (P_b)_x)$ as functions of $(P_a)_x$ and $(P_b)_x$ with all other momentum components set to zero and $\lambda = 5$. Top left panel show the result for V in 2D with $N = 16$, top right for M in 2D with $N = 16$, bottom left for V in 3D with $N = 12$, and bottom right for M in 3D with $N = 12$.

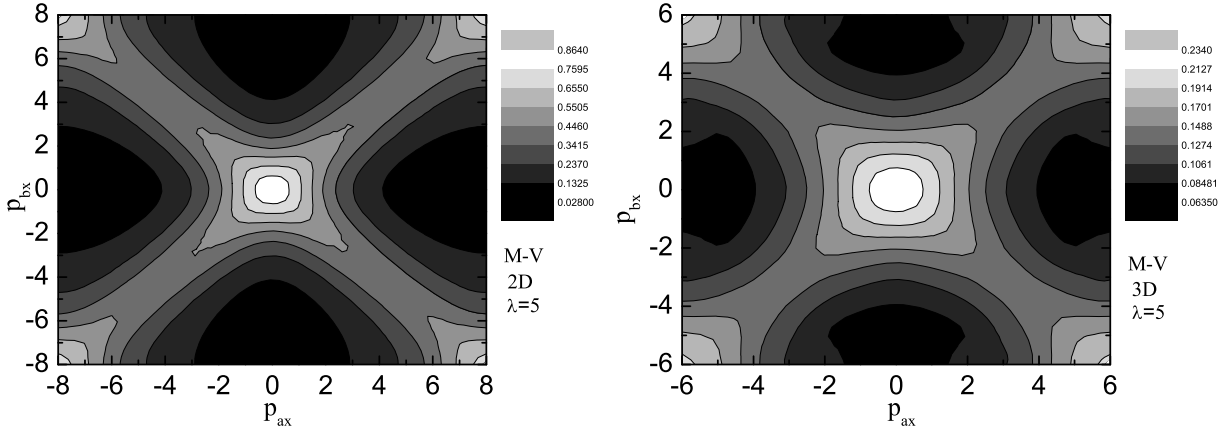


FIG. 10. Contour plot of $M((P_a)_x, (P_b)_x) - V((P_a)_x, (P_b)_x, (P_c)_x = -(P_a)_x)$ with $\lambda = 5$. Calculations are done in 2D with $N = 16$ (left panel) and in 3D with $N = 12$ (right panel).

V. SUMMARY AND OUTLOOK

In this work we have compared the self-consistent 4-point vertex V from 4PI effective action with the BS 4-vertex M from 2PI effective action in 2D and 3D. In order to do the calculation we have developed a technique to fully exploit the symmetries of the 4-vertex V . The difference between V and M depends on the external momenta. We have shown that when V is taken in a diagonal momentum configuration, the two vertices agree well when λ is as large as 5. For non-diagonal momenta, V , M and the perturbative vertex agree well when the coupling strength λ is small, but when the coupling strength is increased the three vertices differ strongly from each other. We conclude that for physical quantities where the physics of the 4-point function is important, but for which diagonal momenta are expected to dominate, accurate results can be expected using the 2PI effective action. In general however, one needs the full non-perturbative 4-point function obtained from the 4PI effective action.

ACKNOWLEDGEMENTS

The authors would like to thank Norm Finlay for invaluable technical assistance.

This work was supported by the Natural and Sciences and Engineering Research Council of Canada. WJF is supported in part by the National Natural Science Foundation of China under Contracts No. 11005138.

-
- [1] E. Braaten and R. D. Pisarski, Nucl. Phys. **B 337**, 569 (1990).
 - [2] J. M. Luttinger and J. C. Ward, Phys. Rev. **118**, 1417 (1960); G. Baym and L. P. Kadanoff, Phys. Rev. **124**, 287 (1961); P. Martin and C. De Dominicis, J. Math. Phys. **5**, 14 (1964); **5**, 31 (1964).
 - [3] J. M. Cornwall, R. Jackiw, and E. Tomboulis, Phys. Rev. **D 10**, 2428 (1974).
 - [4] J. P. Blaizot, E. Iancu, and A. Rebhan, Phys. Rev. Lett. **83**, 2906 (1999), arXiv:hep-ph/9906340; Phys. Rev. **D 63**, 065003 (2001), arXiv:hep-ph/0005003.
 - [5] J. Berges, Sz. Borsányi, U. Reinosa, and J. Serreau, Phys. Rev. **D 71**, 105004 (2005), arXiv:hep-ph/0409123.
 - [6] J. Berges and J. Cox, Phys. Lett. **B 517**, 369 (2001), arXiv:hep-ph/0006160; J. Berges, Nucl. Phys. **A 699**, 847 (2002), arXiv:hep-ph/0105311; G. Aarts and J. Berges, Phys. Rev. Lett. **88**, 041603 (2002), arXiv:hep-ph/0107129; G. Aarts, D. Ahrensmeier, R. Baier, J. Berges, and J. Serreau, Phys. Rev. **D 66**, 045008 (2002), arXiv:hep-ph/0201308.
 - [7] J. P. Blaizot, J. M. Pawłowski, and U. Reinosa, Phys. Lett. **B 696**, 523 (2011), arXiv:1009.6048.
 - [8] G. Aarts and J. M. Martínez Resco, JHEP **02**, 061 (2004), hep-ph/0402192.
 - [9] J. Berges, Phys. Rev. **D 70**, 105010 (2004), arXiv:hep-ph/0401172.
 - [10] G. D. Moore, Proceedings of SEWM 2002, Ed. M.G. Schmidt, arXiv:hep-ph/0211281.
 - [11] M.E. Carrington and E. Kovalchuk, Phys. Rev. **D76**, 045019 (2007), arXiv:0705.0162.
 - [12] M.E. Carrington and E. Kovalchuk, Phys.Rev. **D77**, 025015 (2008), arXiv:0709.0706.
 - [13] R. E. Norton and J. M. Cornwall, Ann. Phys. (N.Y.) **91**, 106 (1975).
 - [14] M.E. Carrington, Eur. Phys. J. **C35**, 383 (2004), arXiv:hep-ph/0401123.
 - [15] M. E. Carrington and Y. Guo, Phys. Rev. **D83**, 016006 (2011), arXiv:1010.2978.
 - [16] M. E. Carrington and Y. Guo, Phys. Rev. **D85**, 076008 (2012), arXiv:1109.5169.
 - [17] M. E. Carrington and E. Kovalchuk, Phys. Rev. **D80**, 085013 (2009), arXiv:0906.1140.
 - [18] M. E. Carrington and E. Kovalchuk, Phys. Rev. **D81**, 065017 (2010), arXiv:0912.3149.
 - [19] H. van Hees, J. Knoll, Phys. Rev. **D65**, 105005 (2002), arXiv:hep-ph/0111193; *ibid* Phys. Rev. **D65**, 025010 (2002), arXiv:hep-ph/0107200.
 - [20] J-P Blaizot, E. Iancu, U. Reinosa, Nucl. Phys. **A736**, 149 (2004), arXiv:hep-ph/0312085.
 - [21] J. Berges, Sz. Borsányi, U. Reinosa, J. Serreau, Annals Phys. **320**, 344 (2005), arXiv:hep-ph/0503240.
 - [22] U. Reinosa, J. Serreau, Annals Phys. **325**, 969, (2010), arXiv:0906.2881.
 - [23] M.C. Abraao York, G.D. Moore, M. Tassler, arXiv:1202.4756.
 - [24] D. Binosi and L. Theussl, Comput. Phys. Commun. **161**, 76 (2004), arXiv:hep-ph/0309015.
 - [25] M. E. Carrington and Wei-Jie Fu, Eur. Phys. J. **C 73**, 2399 (2013), arXiv:1202.3165.